

An Educational Resource for Visualizing the Global Seismic Wave Field

by Michael S. Thorne, H. Philip Crotwell, and Gunnar Jahnke

INTRODUCTION

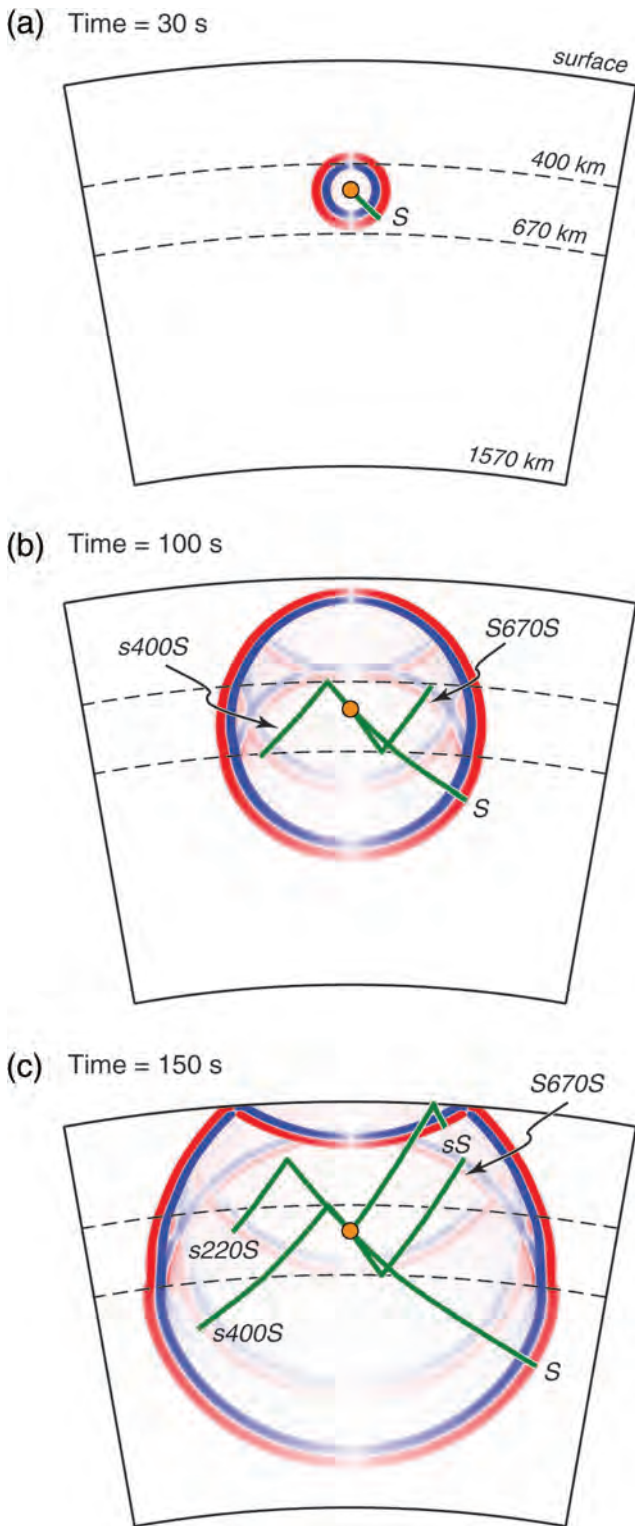
The technology currently available in university classrooms often includes interactive whiteboards, high-definition displays and projectors; furthermore, many students are equipped with tablet computers. Nevertheless, teaching material that can take advantage of these technologies is time consuming to produce and there is need for additional available material for courses in geophysics. The use of dynamic materials, such as animations and movies in the classroom has been shown to have the ability to enhance learning (e.g., see Mayer and Moreno, 2002, for a review). However, traditional methods of teaching about the global seismic wave field typically involve static imagery. Usually this has been achieved through a combination of drawing ray paths and wave fronts at distinct timesteps. Thus, students have had to build the mental connections between the underlying wave propagation and the static imagery being displayed. But the recent availability of cheap computer clusters has made numerical computation of the seismic wave field in realistic Earth models readily accessible. As a result, animating seismic-wave propagation has become relatively commonplace.

Some of the first global animations of seismic-wave propagation were produced by summing torsional mode free oscillations in the mantle to show the SH wave field at periods down to 12 s (Wyssession and Shore, 1994). This set of animations has been a valuable educational resource and has inspired us to create a new collection. Here, we present a new series of global seismic-wave animations that includes both the SH and P/SV wave field. In addition, recent developments to the TauP Toolkit (Crotwell *et al.*, 1999) have made it possible to animate seismic ray paths and wavefronts. Thus, our collection combines the seismic wave field with dynamically drawn ray paths and/or wavefronts. In what follows, we describe a few of the animations that are available on the global scale and some ideas of how these can be used in teaching. The animations are available in high-definition (HD) format with resolutions of 1920×1080 or 1280×720 pixels. The collection is available for download from the website: <http://web.utah.edu/thorne/animations.html>.

SH -WAVE MOTION

In global wave propagation, SH -wave motion in an isotropic medium provides the simplest case to describe. We compute the wave field using the SHaxi technique (Jahnke *et al.*, 2008). The SHaxi method is an axi-symmetric finite-difference (FD) technique. Velocities are input on a 2D grid, and the grid is virtually rotated around an axis passing through the source and the center of the Earth. The utility of this technique is that computations are performed on a 2D grid, but the correct 3D geometrical spreading is retained. For generating wave field animations, this software package can output the seismic velocity at each point in the 2D grid at regularly sampled timesteps. Animations provided on the webpage are computed for a dominant period of 15 s. The Preliminary Reference Earth Model (PREM; Dziewonski and Anderson, 1981) is used as the background model. Animations included on the website are purely elastic except for one animation that compares the effects of elastic to anelastic wave propagation. Animations were generated for source depths of 0 and 500 km. As the majority of the animations provided on the website use the 500 km source depth, we first describe the wave field around the initial timesteps for this deep source. The SHaxi method uses a ring source with amplitude that depends on the sine of the takeoff angle.

Figure 1 shows three snapshots of the SH wave field in the vicinity of the source and provides an excellent starting place for describing these animations in the classroom. Figure 1a shows the wave field 30 s after the source initiates (source location shown with orange circle). Here, the wave field is an SH wave radiating from the source. Particle displacements are in and out of the plane of the page, and are shaded red and blue for positive and negative displacements, respectively. In displaying animations of the seismic wave field a common practice is to use a non-linear color scale. Here, the seismic-wave amplitudes are raised to the power n , where n is chosen in the range of 0.25–0.5. This non-linear color scale makes it easier to see low amplitude arrivals as displayed in the next timestep (time = 100 s) in Figure 1b. Because the source is placed at 500 km depth, reflections are observed from the transition-zone discontinuities (located at 400 and 670 km depths in the PREM model). The phase $s400S$ is the bottom-side reflection off of the 400 km discontinuity, and the $S670S$ phase is a top-side reflection off the 670 km discontinuity. In addition to the transition-zone discontinuities, the PREM model also contains a discontinuity at 220 km depth. This generates a bottom-side reflection, $s220S$, which is seen in Figure 1c. The high amplitude sS reflection from the free surface is also

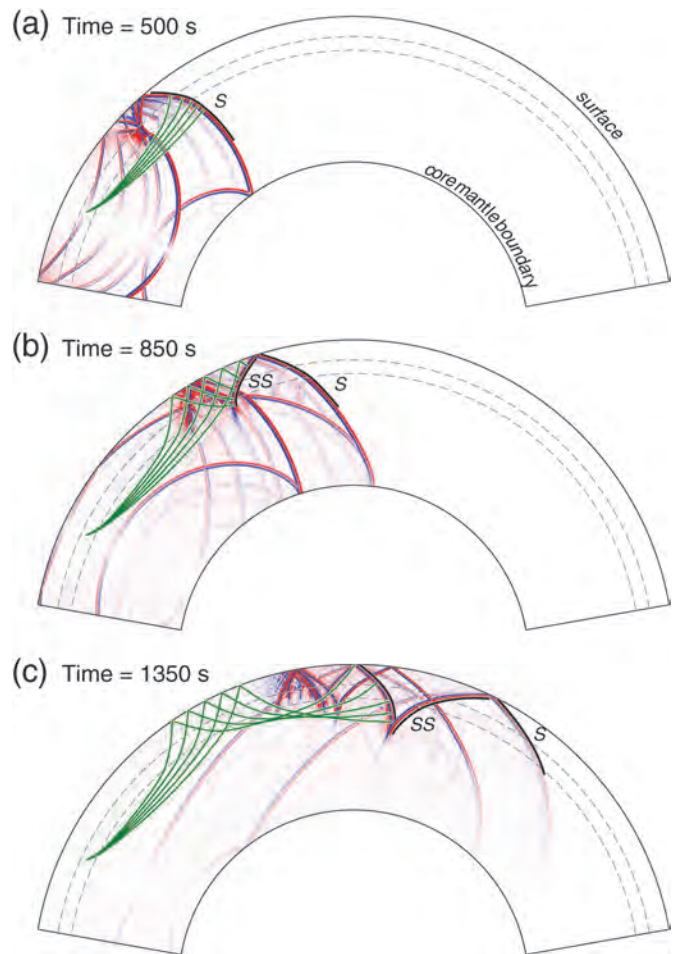


▲ **Figure 1.** *SH*-wave propagation at (a)–(c) three timesteps in the vicinity of the source (orange circle). In each panel the displacement is perpendicular to the plane of the page and is shaded blue and red for motions in and out of the page, respectively. Green lines show ray paths for visible seismic phases where phase names are provided using the TauP Toolkit convention. The area shown is limited in depth from the surface to 1570 km and in the angular range from -10° to $+10^\circ$.

observed in the final timestep. As the majority of *SH*-wave animations on the webpage have a 500 km source depth, it is useful to first describe the seismic phases that we see in the initial timesteps so that at later timesteps we are aware of the origins of the multiple low-amplitude arrivals that are apparent.

There are several excellent teaching opportunities based on these first few timesteps. For example, there is a π -phase shift in *SH* that occurs for the top-side reflection (*S670S*, leading wavefront is now blue where it was formerly red), but does not occur for the bottom-side reflections. In Figure 1c, we can also see the effect of increasing velocity with depth. That is, the wavefront in Figure 1a appears approximately spherical, but by the last timestep (Fig. 1c) the wavefront has grown more oblate as it is expanding faster in the deeper part of the Earth. The effect of the discontinuous velocity jumps in the transition zone also provides a subtle, but noticeable, increase in wavelength that can also be observed as the wavefront expands into the deep mantle.

Another example of *SH*-wave propagation is shown in Figure 2. In this sequence of snapshots, we highlight the



▲ **Figure 2.** *SH* wave field and ray paths highlighting the development of the *SS* wavefront. Ray paths (green lines) are traced for *SSS* arrivals in 10° increments for epicentral distances of 100° to 140° . *S* and *SS* wavefronts are outlined with the heavy black line.

development of the *SS* wavefront. Ray paths for the *SSS* arrivals are drawn for epicentral distances ranging from 100° to 140° in 10° increments. We draw ray paths for *SSS* because this provides us with a tighter grouping of ray paths with which to describe the characteristic *Y*-shape of the wave field that dominates the upper mantle. This *Y*-shape is apparent in the minimax seismic phases, such as *SS*, *SSS*, *SSSS*, and also the *SS* precursor phases, such as *S400S* and *S670S*.

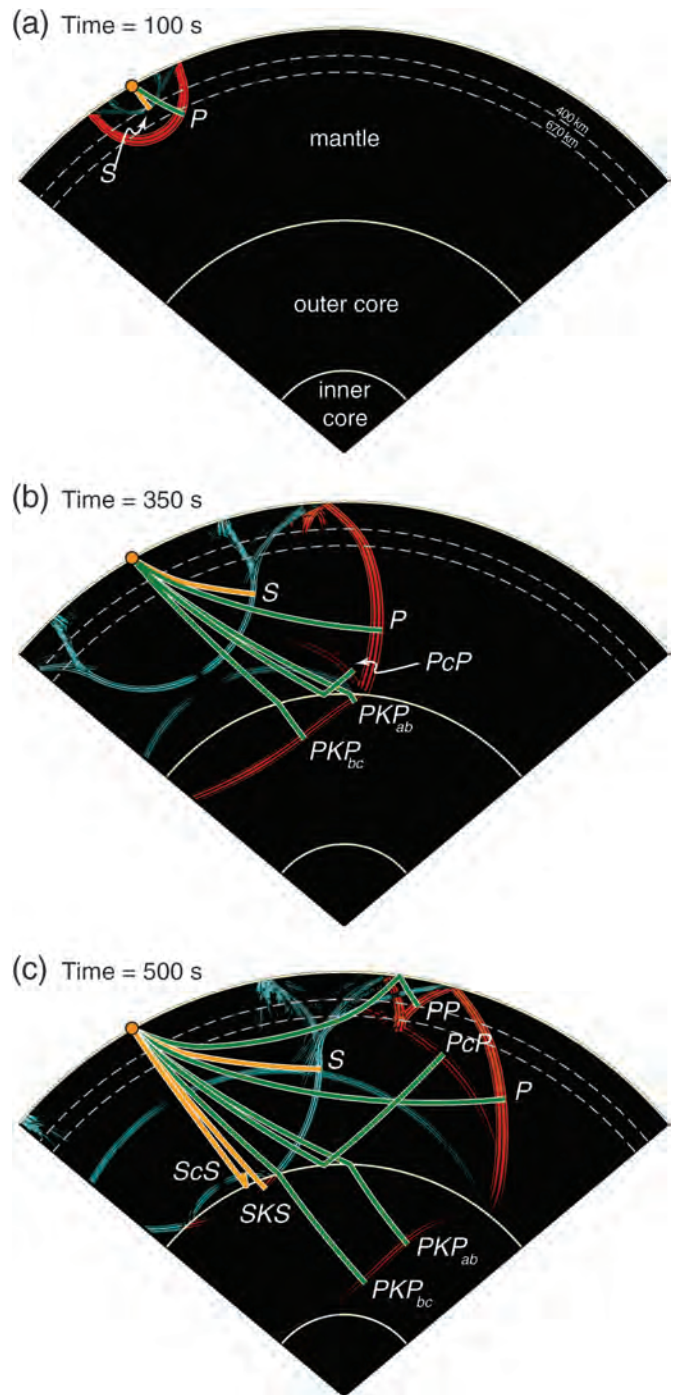
The first timestep shown in Figure 2a (500 s) is drawn after the *S*-wave ray paths have just passed beyond their turning depth. The *S* wavefront (heavy black line) is shown for reference and displays a distinct bend as it crosses into the slower upper mantle. At the second timestep (850 s; Fig. 2b) the ray paths have reflected off of the free surface and are diving back down into the mantle. Here, we see the development of the right branch of the *Y*-shape of the *SS* wavefront. The full *Y*-shape is developed by the third timestep (1350 s; Fig. 2c). Here, the rays are turning back towards the surface and the *Y*-shape has now fully developed. Another teaching opportunity arises in that we can observe the $\pi/2$ phase shift that occurs in the *SS* arrival. If we look at the downgoing *SS* wave field in Figure 2c (right branch of the *Y*) we see first red-, then blue-shaded displacements (i.e., displacements first in, then out of the page). But, the upgoing wave field (left branch of the *Y*) is phase shifted by $\pi/2$, which is apparent in the red-blue-red color sequence. The actual phase shift can first be noted at the bottom branch of the *Y*-shape and occurs where the wave field folds over itself. The development of the *SS* waveshape is much easier to see when combined with dynamically drawn ray paths thus showing the utility of combining both rays and wave field in these animations.

Many more *SH*-wave animations are provided on the website (e.g., highlighting the seismic phases: *SS*, *SS* precursors, *Sdif*, *ScS*, *ScSScS*, and *sS*). Wyssession and Shore (1994) have also provided an excellent description of the *SH* wave field, hence we refer the reader to that paper for further teaching ideas.

P-/SV-WAVE MOTION

The *P/SV* wave field is computed using the *PSVaxi* method (the counterpart to *SHaxi*). The method is based on the technique of Igel and Weber (1996), but has also been updated to run efficiently on supercomputer architectures (Jahnke, 2009; Thorne *et al.*, 2013). *P/SV* animations are also computed for a dominant period of 15 s, using the PREM background model, and source depths of 0 or 500 km.

The passage of a *P* wave through the Earth involves consecutive compression and extension of the traversed materials and we thus observe temporary volume changes. But, the material does not undergo any rotations as the *P* wave passes. On the other hand, the passage of an *S* wave involves temporary rotation of Earth material but does not involve volume changes. We can thus separate out distinct *P*- and *S*-wave motions by calculating the divergence and curl of the wave field. For example, the divergence of the wave field is non-zero where



▲ **Figure 3.** *P/SV* wave field at (a)–(c) three timesteps for a surface source (orange circle). The divergence and curl of the wave field is shaded red and blue, respectively, to highlight *P* and *SV* waves. Selected ray paths for seismic phases that reach the surface as *P* or *SV* waves are drawn with green or yellow lines, respectively.

volume changes exist; hence, in calculating the divergence of the wave field we highlight the *P* waves and suppress the *S* waves. Similarly, if we calculate the curl of the wave field, we highlight the *S* waves and suppress the *S* waves. Figure 3a–c shows three snapshots of *P*-/*SV*-wave propagation in which

we have separately calculated the divergence and curl of the displacement colored in red and blue for P waves and S waves, respectively.

Our first example shown in Figure 3a displays the P/SV wave field in the vicinity of the source and, as with the SH examples explained above, provides a good starting point for describing these animations. The first timestep (Fig. 3a) shows the wave field for a surface source (actual depth is 0.1 km) after 100 s. Here, we see the faster P wave (shaded in red, with green ray path) well ahead of the S wave (shaded in blue, orange ray path). As noted above, the computation is done with a source-time function that has a dominant period of 15 s. Hence, we can see that the P wave has a longer wavelength as it is propagating through material which has larger wave speeds. At the second timestep (Fig. 3b; 350 s) the downgoing P wave has crossed the core–mantle boundary (CMB). At this timestep we see the development of the PKP arrival, separately labeled as PKP_{ab} and PKP_{bc} branches. The downgoing P waves slow dramatically as they enter the outer core (ray paths bend away from the CMB) and there is a decrease in the wavelength. Furthermore, both the core-reflected PcP arrival and core-converted phase PcS are observed. The S wave still lags in the mid-mantle. At the final timestep (Fig. 3c; 500 s) the S wave has reached the CMB and we can see the ScS reflection as well as a conversion to a P wave in the outer core, which is the start of the SKS arrival. In the upper mantle we can also see the characteristic Y -shape of the minimax arrivals starting to develop, in this case for the PP arrival. In addition to describing the seismic arrivals other teaching opportunities include: (1) differences in P - and S -wave speeds, (2) variations in seismic wavelength, and (3) P -to- S and S -to- P conversions at boundaries, including the CMB.

These animations help to demonstrate the relationships among various seismic phases. An example is provided in Figure 4 in which we show a zoomed-in region of the wave field near the CMB. Two of the seismic phases often utilized in studying fine-scale deep mantle layering (e.g., ultra-low velocity zones, ULVZs) are ScP and $SPdKS$ (e.g., Thorne and Garnero, 2004). $SPdKS$ starts off as an ScP wave that strikes the CMB at the critical angle for P -wave diffraction, the development of which is shown in Figure 4. The left column of Figure 4 shows the divergence (red) and curl (blue) of the wave field to highlight P - and SV -wave energy, respectively. The right column shows a cartoon of the visible wave fronts. In the first panel (Fig. 4a; 370 s) we observe the downgoing S -wave energy reflecting off the CMB and generating an ScP arrival. In the next timestep (Fig. 4b; 410 s), the ScP energy is both upgoing and diffracting along the CMB. Another timestep later (Fig. 4c; 450 s), we can see the full relation between these phases as the upgoing ScP energy merges into the diffracting SPd energy, which can also be seen diving into the outer core as $SPdK$, ultimately becoming an $SPdKS$ arrival. Analyzing the wave field as shown in Figure 4 is exceptionally useful in visualizing how the wave field interacts with small-scale CMB structures such as ULVZs. Furthermore, from a research point

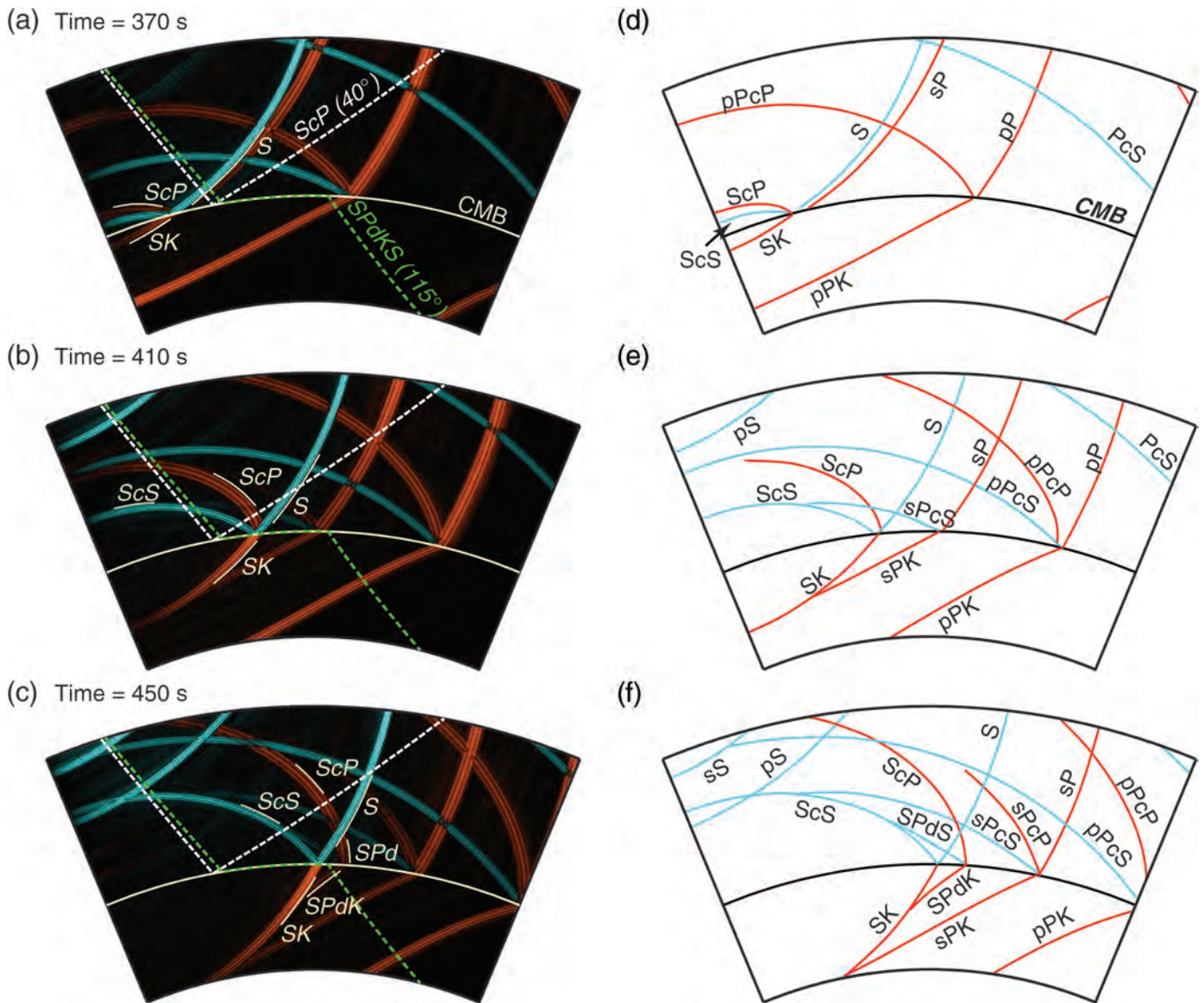
of view, it can be invaluable in determining the origin of arrivals apparent in seismograms.

THE MOON

An interesting contrast to the wave fields shown for the Earth in the previous sections is provided by examining wave propagation in the Moon. Multiple 1D seismic-velocity models have been constructed for the Moon since the early 1970s. These models have revealed an average seismic structure containing a 20–40 km thick crust, which overlays a nearly homogeneous lunar mantle that extends down to depths of at least 1000 km. Here, we generate animations using the Very Preliminary REference MOON model (VPREMOON; Garcia *et al.*, 2011). This model has a 28 km thick crust ($V_P = 3.2$ – 5.5 km/s; $V_S = 1.8$ – 3.3 km/s) overlaying a nearly homogeneous mantle. The mantle model includes a slight increase in velocity with depth (V_P goes from 7.54 to 8.23 km/s from 28 to 1357 km depths; V_S goes from 4.34 to 4.64 km/s over the same range). Also included in this model is a 380 km thick core. Most lunar models contain a 1 to 2 km thick layer with extremely low wave speeds (e.g., $V_P = 1$ km/s and $V_S = 0.5$ km/s in VPREMOON). However, in order to reduce computation time we do not include this layer in these animations. Wave-field calculations are done using a modified version of SHaxi gridded for the Moon. Several shallow moonquakes (depths less than roughly 200 km) have been recorded on the Moon (see, e.g., Lognonné *et al.*, 2003). Yet, the majority of recorded moonquakes had deep sources occurring in a depth range from roughly 550 to 1400 km (e.g., Nakamura, 2005). Hence, animations on the website are calculated for a shallow source depth of 5 km and a deep moonquake source at 700 km. All lunar wave-field calculations are done for a 10 s dominant period (as opposed to 1 s dominant period of recorded lunar seismic energy) in order to make the wave field easier to see.

Figure 5a–c shows three snapshots of wave propagation through the VPREMOON model for a 700 km deep moonquake. In Figure 5a, we see a simple SH wave radiating from the source. As the Moon’s mantle is nearly homogeneous, the SH wavefront is almost circular and the ray path shown is nearly a straight line. This is in contrast to wave propagation in the Earth at a similar timestep (Fig. 1b), in which we are already able to see a significant bending of the ray paths and elongation of the wave fronts due to the increasing wave speed with depth.

In the second timestep (Fig 5b, time = 150 s), we see the development of the core-reflected ScS arrival. We also see multiple arrivals reflected near the surface. The strongest arrival is the sS phase, but we also see strong reflectors from the underside of the two-layer crust preceding the sS phase. The S -wave velocity increase at the base of the lunar crust is roughly 32% (or almost twice as strong as the Earth’s crust–mantle S -wave increase of 15%), but there is a huge 83% increase in S -wave velocity in the mid-lunar crust. This low-velocity crust creates multiple strong reverberations that are seen in the third timestep (Fig 5c; 325 s). The crustal reverberations continue well



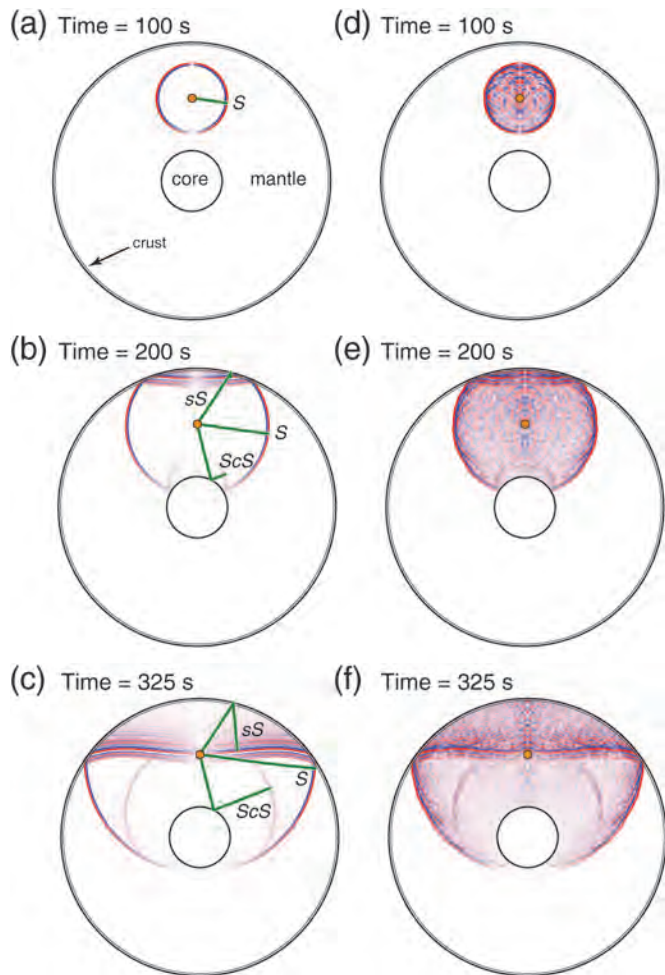
▲ **Figure 4.** *P/SV* wave field at three timesteps for a deep (500 km) source zoomed in to show detail near the Earth's core–mantle boundary. (a)–(c) The wave field (divergence and curl colored red and blue, respectively). Additionally, ray paths for an *ScP* arrival at 40° and an *SPdKS* arrival at 115° are shown for reference. Selected wavefronts are highlighted in white. (d)–(f) The seismic phases visible in each snapshot.

after the direct *S* wave, thus contributing to a long train of arrivals in the tail, or coda, of the *S* wave.

One of the primary features of lunar seismograms is the long duration of the seismic coda (on the order of 3600 s). The long duration of the lunar coda is due to a combination of low lunar attenuation, which is expected if the Moon lacks water, and the existence of strong scatterers of seismic energy (e.g., Dainty and Tököz, 1981). We illustrate this case in Figure 5d–f, in which we have added small-scale random velocity perturbations to VPREMOON to simulate scatterers. Here, we add *S*-wave velocity perturbations to the entire lunar model characterized by a 10 km autocorrelation length, an exponential autocorrelation function, and 3% root mean square velocity perturbations.

Here, the choice of autocorrelation function primarily affects the roughness of the model, which affects the strength of seismic scattering at wavelengths that are approximately less than the autocorrelation length. (see Frankel and Clayton, 1986, for definitions of these terms and examples of other autocorrelation functions).

Figure 5d shows the wave field at the first timestep (compare with Fig. 5a; same timestep, but no velocity perturbations). The primary difference in the case with scattering is that we see small aberrations in the *SH* wavefront and additional seismic energy tailing the primary arrivals. In other words, the wavefront is no longer nearly circular, but appears bumpy as the wave travels through randomly varying seismic



▲ **Figure 5.** Snapshots of SH -wave propagation in the Moon. (a)–(c) Three snapshots for the VPREAMOON model. (d)–(f) Three snapshots at identical timesteps for VPREAMOON with added small-scale random velocity perturbations. Orange circle, Deep moonquake source used (at 700 km depth). Green lines, ray paths for the S , ScS , and sS seismic phases.

velocities either speeding up or slowing down the wavefront. In addition, seismic coda has developed behind the main SH wave as this wave is being reflected off of the many small-scale velocity perturbations. In the final timestep (Fig. 5f), we see that observing core-reflected phases on the Moon, such as ScS , can be exceptionally challenging due to interference with both scattered seismic energy and the multiple crustal reverberations. Another pedagogical point apparent from these examples is to show that one of the reasons why computed synthetic seismograms appear so clean compared to actual data: Synthetic models typically do not contain small-scale heterogeneity that causes seismic scattering and coda development in the real Earth or Moon. Thus, real data contains many smaller seismic arrivals that may arise from wave-field interactions with as yet unmapped structural features or small-scale heterogeneity below the detection threshold of modern seismic methods.

SUMMARY

We have presented a collection of animations that show global wave propagation in both the Earth and the Moon. These animations are accessible from the web (<http://web.utah.edu/thorne/animations.html>), as are a series of regional scale animations, not discussed in this paper, that demonstrate key concepts in seismic-wave propagation, such as the development of headwaves, diffraction, and interaction with small-scale velocity anomalies. We point out that animations such as these also have value as a research tool, as these animations tend to make us think in terms of the actual seismic waves that are interacting with structure as opposed to geometric rays. However, it is anticipated that these animations will primarily be used in the classroom as a teaching aid. An important point is that these animations can be stopped at key frames so the evolution of the waveform features can be discussed in detail. Furthermore, some current technologies available in the classroom, for example, tablet devices or interactive whiteboards, make it possible to add freehand sketches (think of the telestrator in sports broadcasting) on top of the animations. Combined with narration, this can create an effective method for helping students to build the mental connections between static ray paths and the underlying wave propagation and to build intuition about what seismic waves do when interacting with seismic-velocity structures on a global scale. ☒

ACKNOWLEDGMENTS

We gratefully acknowledge the University of Utah Center for High Performance Computing (CHPC) for computer resources and support. MT was partially supported by NSF Grants EAR-1014749, EAR-0952187 and NASA Grant NNX11AH47G. We thank K. Koper and Editor A. Kafka for their constructive review and suggestions. Animations and figures were generated using the Generic Mapping Tools (<http://gmt.soest.hawaii.edu/>; Wessel and Smith 1998), ImageMagick (<http://www.imagemagick.org/>), and POV-Ray (<http://www.povray.org>).

REFERENCES

- Crotwell, H. P., T. J. Owens, and J. Ritsema (1999). The TauP Toolkit: Flexible seismic travel-time and ray-path utilities, *Seismol. Res. Lett.* **70**, 154–160.
- Dainty, A. M., and M. N. Tököz (1981). Seismic codas on the Earth and the Moon: A comparison, *Phys. Earth Planet. In.* **26**, 250–260.
- Dziewonski, A. M., and D. L. Anderson (1981). Preliminary Reference Earth Model, *Phys. Earth Planet. In.* **25**, 297–356.
- Frankel, A., and R. W. Clayton (1986). Finite difference simulations of seismic scattering: Implications for the propagation of short-period seismic waves in the crust and models of crustal heterogeneity, *J. Geophys. Res.* **91**, no. B6, 6465–6489.
- Garcia, R. F., J. Gagnepain-Beyneix, S. Chevrot, and P. Lognonné (2011). Very preliminary reference Moon model, *Phys. Earth Planet. In.* **188**, 96–113, doi: 10.1016/j.pepi.2011.06.015.
- Igel, H., and M. Weber (1996). P-SV wave propagation in the Earth's mantle using finite differences: Application to heterogeneous lowermost mantle structure, *Geophys. Res. Lett.* **23**, no. 5, 415–418.

- Jahnke, G. (2009). *Methods for Seismic Wave Propagation on Local and Global Scales with Finite Differences*, Ludwig-Maximilians-Universität, München, Germany, 99 pp.
- Jahnke, G., M. S. Thorne, A. Cochard, and H. Igel (2008). Global SH-wave propagation using a parallel axisymmetric spherical finite-difference scheme: Application to whole mantle scattering, *Geophys. J. Int.* **173**, no. 3, 815–826, doi: 10.1111/j.1365-246X.2008.03744.x.
- Lognonné, P., J. Gagnepain-Beyneix, and H. Chenet (2003). A new seismic model of the Moon: Implications for structure, thermal evolution and formation of the Moon, *Earth Planet. Sci. Lett.* **211**, 27–44, doi: 10.1016/S0012-821X(03)00172-9.
- Mayer, R. E., and R. Moreno (2002). Animation as an aid to multimedia learning, *Educ. Psychol. Rev.* **14**, no. 1, 87–99.
- Nakamura, Y. (2005). Farside deep moonquakes and deep interior of the Moon, *J. Geophys. Res.* **110**, E01001, doi: 10.1029/2004JE002332.
- Thorne, M. S., and E. J. Garnero (2004). Inferences on ultralow-velocity zone structure from a global analysis of SPdKS waves, *J. Geophys. Res.* **109**, B08301, doi: 10.1029/2004JB003010.
- Thorne, M. S., Y. Zhang, and J. Ritsema (2013). Evaluation of 1D and 3D seismic models of the Pacific lower mantle with S, SKS, and SKKS traveltimes and amplitudes, *J. Geophys. Res.* **118**, 1–11, doi: 10.1002/jgrb.50054.
- Wessel, P., and W. H. F. Smith (1998). New, improved version of Generic Mapping Tools released, *Eos Trans. AGU* **79**, no. 47, 579.
- Wyssession, M. E., and P. J. Shore (1994). Visualization of whole mantle propagation of seismic shear energy using normal mode summation, *Pure Appl. Geophys.* **142**, 295–310.

Michael S. Thorne
Department of Geology and Geophysics
University of Utah
Salt Lake City, Utah 84112 U.S.A.
michael.thorne@utah.edu

H. Philip Crotwell
Department of Geological Sciences
University of South Carolina
Columbia, South Carolina 29208 U.S.A.

Gunnar Jahnke
SMA Solar Technology AG
Sonnenallee 134266
Niestetal, Germany